Transverse modes in thermally detuned oxide-confined vertical-cavity surface-emitting lasers

C. Degen, I. Fischer, and W. Elsäßer
Institute of Applied Physics, Darmstadt University of Technology, Schloßgartenstrasse 7, 64289 Darmstadt, Germany

L. Fratta, P. Debernardi, and G. P. Bava
Dipartimento di Elettronica, Istituto di Ricerca sull' Ingegneria delle Telecomunicazioni e dell' Informazione, Politecnico di Torino, Istituto Nazionale per la Fisica della Materia,Unita' di Ricerca di Torino, Corso Duca degli Abruzzi, 24, 10129 Torino, Italy

M. Brunner, R. Hövel, M. Moser, and K. Gulden
Avalon Photonics, Badenerstrasse 569, 8048 Zürich, Switzerland
(Received 17 May 2000; published 18 January 2001)

We present joint experimental and theoretical investigations of the emission characteristics of oxide-confined vertical-cavity surface-emitting lasers (VCSEL's). The transverse mode formation in medium-sized VCSEL's is determined by the interaction between spatial cavity characteristics and spectral properties of the optical gain: depending on a detuning between the cavity fundamental resonance and the spectral gain maximum, we find the VCSEL's emitting either on the fundamental transverse mode or on modes of particularly high radial order. For a quantitative interpretation of these characteristics, we adopt a model that considers the detailed electromagnetic structure of the VCSEL and yields wavelength, spatial field distribution, and threshold gains of all supported cavity modes. Combining these solutions with the quantum-well optical response provides the laser threshold operation conditions. The theoretical results are in excellent quantitative agreement with the experimental observations. Thus, our work identifies the relevant mechanisms and offers the perspective to control and to utilize high-order mode emission from oxide-confined VCSEL's.

DOI: 10.1103/PhysRevA.63.023817 PACS number(s): 42.55.Px, 42.55.Sa

I. INTRODUCTION

Vertical-cavity surface-emitting lasers (VCSEL's) have a huge potential for future technological applications. Their low threshold currents, high modulation bandwidth, and inherent longitudinal single-mode emission make them the ideal light sources for optical information transmission [1,2]. Moreover, astigmatism-free circular beam profiles and the possibility of easy two-dimensional integration open up manyfold possibilities from optical storage and image recording to large-scale display applications [3]. The most highly developed VCSEL's today are oxide-confined devices, in which a selectively oxidized layer of high aluminum content serves for both optical and electrical confinement [4]. On one hand, the oxide confinement has significantly improved the optical and electrical performances; on the other hand, the fully three-dimensional extension of the VCSEL cavity together with the transverse device structure introduced by the oxide layer results in numerous new effects, which make these VCSEL's challenging systems for fundamental physics investigations. Consequently, extensive work has been carried out on quantum noise [5–7], polarization dynamics [8–10], and pattern formation [11] in these lasers. Still, many aspects of the particular emission properties are not completely understood, because of the complex interaction between the device geometry, optical field, and gain medium.

One of these aspects is the formation of spatial modes in oxide-confined VCSEL's [12]. From an applications point of view, this phenomenon gives rise to undesirable effects, such as broadening of the optical spectrum and degradation of the free-space performance due to an excess beam divergence. Therefore, control of the emission characteristics is a desirable goal for, e.g., broad-area high-power VCSEL's [13] or for the application of VCSEL's in multimode-fiber data links [14]. Besides this applications-oriented aspect of multimode VCSEL's, insight into the underlying spatiospectral interactions from the perspective of microscopic physics requires detailed investigations on a fundamental level. One mechanism that can enhance the emission of high-order transverse modes is the detuning between the quantum-well spectral gain maximum and the cavity fundamental resonance [15–20]. The effect, however, critically depends on the strength of the confinement mechanism of the particular device structure: individual technological parameters of the laser can very selectively enhance particular sets of transverse modes [21–23]. Generally, the spatial mode selection in VCSEL's is a complex process due to the interplay of very different mechanisms, and a deep understanding of the emission characteristics can only be obtained by a detailed analysis that considers all significant structural properties as well as fundamental quantum optical mechanisms.

In this paper we present a joined experimental and theoretical approach to identify the mechanisms that govern the transverse mode selection in oxide-confined VCSEL's. Our analysis considers both the fully three-dimensional electromagnetic structure of the device and the spectral gain characteristics of the multiple-quantum-well active region.

In particular, we have performed comprehensive experimental investigations, from which we obtain detailed data on the spectral and spatial emission characteristics of the laser. Depending on injection current and device temperature, we find two distinct operation regimes, which are determined by the emission of low-order transverse modes and by modes of

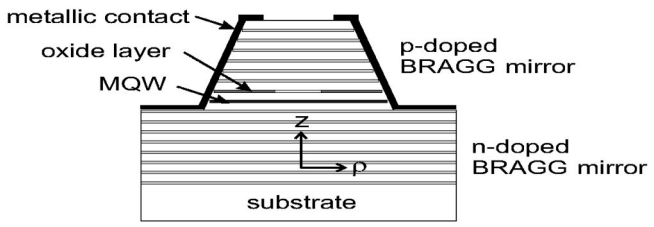

FIG. 1. Scheme of the VCSEL structure.

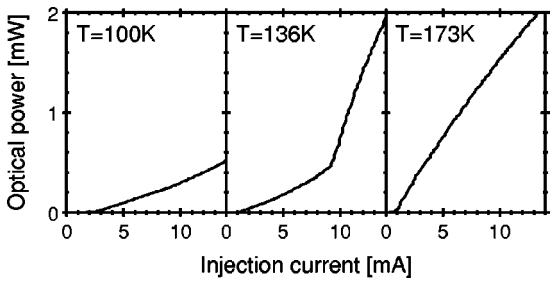

FIG. 2. *P-I* curves at three temperatures.

particularly high radial order, respectively. In order to provide a quantitative understanding of these emission characteristics, we have adopted a model in which the detailed electromagnetic structure of the particular device is considered [24]. The model results in the spatial field distributions, frequency, and threshold gains of all cavity modes. Combining these mode solutions with the optical response of the quantum well then yields the VCSEL's threshold operation conditions. The results of this treatment are in excellent quantitative agreement with the experimental observations, which enables us to identify the relevant fundamental mechanisms underlying the VCSEL's mode formation and so to offer the perspective for controlling the emission characteristics by changing either the operation conditions or the technological device parameters.

The paper is organized as follows. In Sec. II A, we sketch the experimental setup and the structure of the VCSEL's under investigation. Section II B then contains the results of our experimental investigations. In Sec. III, we briefly revise the main features of the adopted theoretical model. The discussion of the numerical results and direct comparison with the results from the experiments follows in Sec. IV. Conclusions are drawn in Sec. V.

II. EXPERIMENTAL PART

A. VCSEL structure and experimental setup

The lasers under investigation are circular oxide-confined GaAs-based VCSEL's of the same structure as those described in [25]. A schematic depiction of the device under analysis is shown in Fig. 1. It is essentially a GaAs λ cavity with two doped highly reflective Bragg mirrors: the top mirror is composed of 22 pairs of *p*-doped $\lambda/4\,Al_{0.9}Ga_{0.1}As/GaAs$ layers, with transverse dimensions defined by the mesa diameter $d_M = 20.6\,\mu$m, while the bottom mirror is composed of 30 pairs of *n*-doped λ/4 layers of the same materials. The metal contact ring on top of the *p*-doped mirror has internal and external diameters amounting to $d_{in} = 8.6\,\mu$m and $d_{ex} = 16.6\,\mu$m, respectively. Wiring and bond pads are evaporated at the end of the technology process.

The active region consists of three 8-nm-thick strained $In_{0.12}Ga_{0.88}As$ quantum wells (QW's). The transverse confinement of the carriers in the active region is achieved by means of a thin circular diaphragm of oxidized AlAs of refractive index $n = 1.6$ [26,27], incorporated into the second $Al_{0.9}Ga_{0.1}As$ layer of the *p*-doped mirror above the cavity. The aperture diameter is $d_A = 10\,\mu$m. We have chosen VCSEL's, in which at room temperature the spectral gain maximum ($\lambda = 966$ nm) is intentionally detuned from the cavity fundamental resonance at $\lambda = 931$ nm. The optimum operating temperature, where both wavelengths match, amounts to $T \approx 170$ K. Hence, we operate the VCSEL's in a liquid-nitrogen-cooled cryostate with built-in electrical heating, which allows us to continuously access temperatures of $T = 90-300$ K and thus to cover both positive ($\lambda_{cavity} > \lambda_{QW}$) and negative ($\lambda_{cavity} < \lambda_{QW}$) detuning conditions.

The injection current is delivered by a commercial constant current source. Power measurements are carried out with a broad area Si–*p-i-n* photodiode in the far field without any optical elements in the beam. For spectral characterization, we focus the light into a grating spectrometer (Jarrel-Ash) by using an aspheric lens [New Focus, numerical aperture (NA) equal to 0.5]. The spectral resolution amounts to 0.25 nm at $\lambda \approx 900$ nm. The near-field images have been recorded with a cooled CCD camera (Apogee) using the same aspheric lens to project the near field onto the CCD array. Possible experimental limitations due to insufficient NA will be discussed in Sec. IV. For the far-field analysis we have placed a semitransparent screen at a distance of 10 cm from the laser. The image of the far field on the screen has then been recorded using a 28-mm focal distance objective. A scale for the far-field images has been obtained from the image of a ruler at the same position as the screen, while a scale for the near fields is given by comparison with images of the VCSEL surface under external illumination, so that the known dimensions of the contact ring and the mesa diameter serve as reference measures.

B. Experimental results

The VCSEL emission characteristics are significantly determined by substrate temperature and injection current. In this parameter space, we categorize the emission into two regimes, in which we find fundamentally different emission with respect to threshold currents, spectral properties, and spatial structure of near field and far field, as will be presented in this section.

The VCSEL optical power characteristics as a function of injection current (*P-I* curve) at three temperatures are depicted in Fig. 2. At $T = 100$ K, the threshold current amounts to $I_{th} = 2.5$ mA and the *P-I* curve is almost linear for $I > I_{th}$. Increasing the temperature to $T = 136$ K results in a qualitatively different behavior: after the primary threshold at $I_{th,I} = 1$ mA, a secondary threshold is reached at $I_{th,II} = 9$ mA, with the slope of the *P-I* curve being significantly larger above the secondary threshold. The different slopes

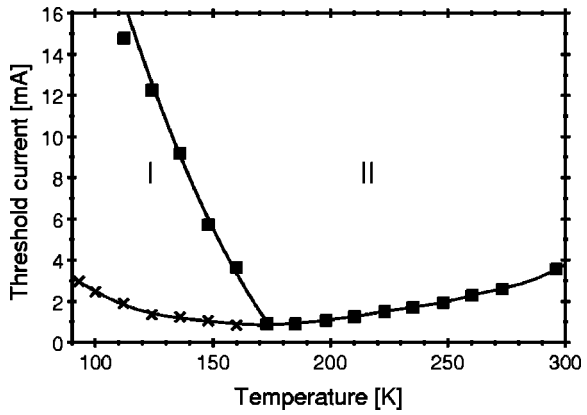

FIG. 3. Threshold currents vs substrate temperature. Full squares indicate low divergence emission (regime II), crosses indicate high divergence modes (regime I).

are caused by strongly different divergence angles of the emission in the respective regimes as will be evidenced later in this section. Since the photodetector is placed directly in the VCSEL's far field, we can use the resulting change in collection efficiency as a probe for a change in the emission characteristics. With further increased temperature, $I_{\mathrm{th,II}}$ decreases and tends towards $I_{\mathrm{th,I}}$, until $I_{\mathrm{th,II}}$ coincides with $I_{\mathrm{th,I}}$ at $T=173\,\mathrm{K}$.

For a better understanding of the laser thermally dependent threshold behavior, we plot $I_{\mathrm{th,I}}$ and $I_{\mathrm{th,II}}$ versus the substrate temperature in Fig. 3. The minimum threshold current of 0.85 mA is obtained at $T=173\,\mathrm{K}$. The crosses indicate the primary threshold, while the squares indicate the secondary threshold. The lines are a guide to the eye and have been obtained by spline regression. They mark the borders of two emission regimes, in the following referred to as regime I and regime II. A transition between the regimes can be obtained ''horizontally'' by changing temperature at constant injection current, and ''vertically'' by changing injection current at constant ambient temperature. In the latter case, the laser internal temperature is raised by Joule heating. The two regimes are characterized by distinctly different spatial and spectral properties as will be discussed in the following.

In Fig. 4, we depict images of far fields and near fields of the VCSEL in the two operating regimes and near the transition. At $T=112\,\mathrm{K}$ and $I=6.0\,\mathrm{mA}$, i.e., in regime I, the far field is determined by a system of concentric rings [Fig. 4(a)]. The full-divergence angle of the outer ring amounts to 70°, which is remarkably large for a VCSEL of 10-μm oxide aperture diameter [28]. Inside the strong outer ring, three additional rings are visible, which exhibit a vague azimuthal structure. The corresponding near field is displayed in Fig. 4(b), with the white circle indicating the aperture of the top metal contact ring, 8.6 μm in diameter. The diameter of the oxide aperture (not visible) is slightly larger and amounts to 10 μm. All intensity in the near field is completely confined within the ring aperture and exhibits a rich structure, indicating a superposition of numerous high-order transverse modes. The spatial structure of both, near field and far field, changes fundamentally when approaching the transition between regime I and regime II, as depicted in Figs. 4(c) and

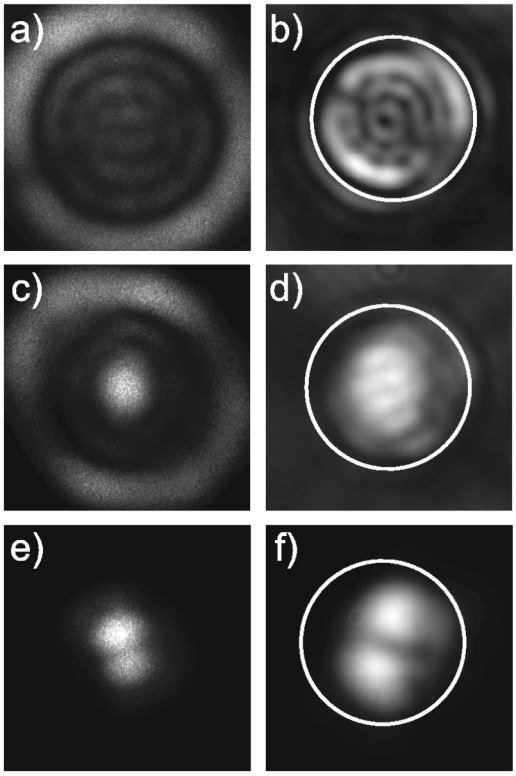

FIG. 4. Far-field (left column) and near-field (right column) images in regime I at $T=112\,\mathrm{K}$, $I=6.0\,\mathrm{mA}$ (a,b), in the transition between the regimes at $T=136$, $I=7.5\,\mathrm{mA}$ (c,d), and in regime II at $T=136\,\mathrm{K}$, $I=10\,\mathrm{mA}$ (e,f). The images are encoded in a linear scale with white corresponding to highest intensity.

4(d) for $T=136\,\mathrm{K}$ and $I=7.5\,\mathrm{mA}$. In the far field, a low divergence spot with full divergence angles of 16° (horizontal) and 24° (vertical) appears in the center of the outer ring, which remains at high divergence. The low divergence spot corresponds to the fundamental transverse mode in the near field, which is superimposed with a still present weak high-order mode, corresponding to the outer ring in the far field. Finally, in regime II at $T=136\,\mathrm{K}$ and $I=10.0\,\mathrm{mA}$, the far field consists of the low divergence part only [Fig. 4(e)], which is the superposition of the fundamental Gaussian mode and the two-lobed first-order transverse mode, also evident in the near field [Fig. 4(f)].

The general interpretation that the spatial structure in near field and far field arises from transverse modes of low order in regime II and modes of remarkably high order in regime I is further supported by the following results from spectral measurements of the VCSEL's emission. In Fig. 5, we plot the optical spectra at $T=112\,\mathrm{K}$ and $I=3\,\mathrm{mA}$, $T=136\,\mathrm{K}$ and $I=8\,\mathrm{mA}$, and $T=160\,\mathrm{K}$ and $I=4\,\mathrm{mA}$ corresponding to regime I, the transition regime, and regime II. In regime I, the emission at $\lambda=913.8\,\mathrm{nm}$ dominates the spectrum with a side mode suppression ratio of 15 dB. This line corresponds to a single lasing high-order transverse mode and it marks the short-wavelength cutoff of a series of subthreshold modes that are visible up to $\lambda\approx 922\,\mathrm{nm}$ with a suppression ratio of approximately 20 dB. In the transition regime, we find two spectral ranges of emission: four high-order modes are ob-

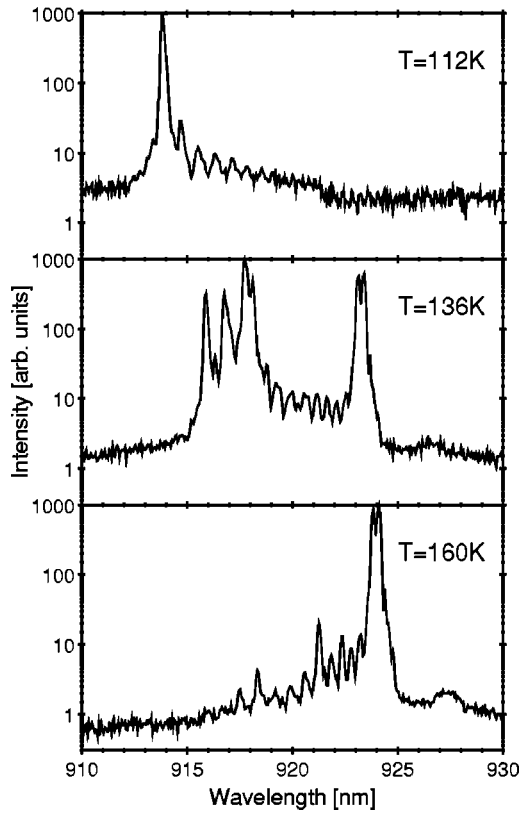

FIG. 5. Laser spectra in the two operation regimes and during the transition in logarithmic depiction.

served from $\lambda = 915.9$ to 918.1 nm, and the fundamental and first-order mode appear around $\lambda = 923.3$ nm. Numerous subthreshold modes are present at intermediate wavelengths. The spectral gap between the shortest wavelength mode and the long-wavelength cutoff of the spectrum amounts to 7.4 nm. Finally, in regime II the fundamental and first-order modes around $\lambda = 924.1$ nm are lasing and subthreshold modes are again suppressed by more than 20 dB.

We depict this thermal dependence of the VCSEL's optical spectrum in Fig. 6 by plotting the wavelengths of the four strongest modes recorded at $I = 3$ mA and varying temperatures between $T = 100$ and 210 K. From $T = 100$ to 136 K, the wavelength of the dominant mode λ_I shifts continuously with a rate of 0.050 nm/K (regime I) due to the thermal shift of the longitudinal cavity resonance caused by the thermal variation of the index of refraction and mechanical expansion of the cavity [29]. Then, at $T = 142$ K, the strongest mode jumps to a 1.3-nm longer wavelength. Next, between $T = 148$ and 155 K, an abrupt transition is observed where the main emission changes by 6.7 nm to $\lambda = 923.3$ nm, corresponding to regime II. During the transition, no intermediate transverse modes are observed. For $T > 155$ K, the wavelength of the dominant mode, λ_{II} shifts again continuously by 0.055 nm/K, following the thermal shift of the fundamental cavity resonance.

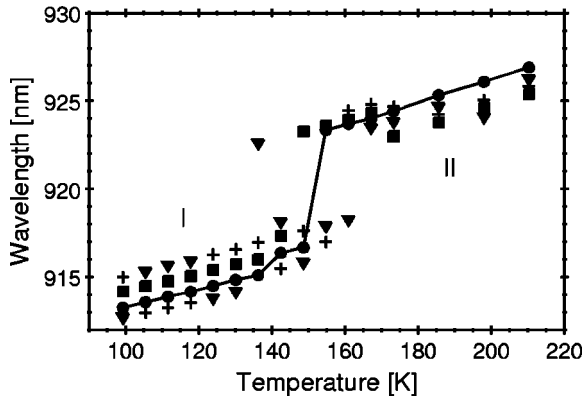

FIG. 6. Wavelength of the four strongest modes; the modes are labeled by full circles connected by the solid line, full squares, crosses, and full triangles, in the order of decreasing intensity.

From all these observed emission characteristics, it is evident that the VCSEL emits in two distinct regimes. In regime I, corresponding to low substrate temperature and low injection current, i.e., at low active region temperature, the laser emits only high-order transverse modes. The large divergence of the far fields corresponds to a remarkably large transverse component of the k vector and thus indicates modes of high radial order. Since the far-field divergence remains constant under variations of temperature, we conclude that modes of one particular radial order are dominant in regime I. The preference of high-order transverse modes is basically determined by the thermally induced detuning between the cavity resonance and the QW spectral gain maximum (positive detuning in regime I, $\lambda_{cavity} > \lambda_{QW}$): the high-order modes near λ_I more efficiently exploit the optical gain and low-order modes at wavelengths near the transverse fundamental resonance are suppressed in this regime. The thermal shift of the emission wavelength in regime I is only determined by the thermal expansion of the cavity and the thermal increase of the optical index.

In regime II, where the active region temperature is higher due to increased substrate temperature or due to Joule heating by increased injection current, the cavity is negatively detuned with respect to the QW gain maximum ($\lambda_{cavity} < \lambda_{QW}$). Here, the VCSEL emits predominantly in the fundamental transverse mode, because it is the mode of longest wavelength, which better matches the spectral gain maximum. Consequently, the near fields are only weakly structured and the far fields exhibit a low divergence, as is usual for oxide-confined devices of comparable size. Again, the thermal shift of the emission wavelength is merely determined by the thermal shift of the longitudinal cavity resonance, with the emission in regime II being about 7.5 nm at longer wavelengths than in regime I.

Somehow similar emission characteristics have been reported recently from broad aperture VCSEL's [18,19]. The basic interpretation of a detuning between the cavity resonance and the QW spectral gain maximum applies to both our measurements and the ones on broad area devices. However, a fundamental difference between these results and our observations is that in broad area devices, emission on higher-order modes is not clamped to a particular mode family, as in our lasers, but a continuous transition to modes of successively increasing order is found for increasing positive detuning. This behavior is determined only by the spectral

properties of the QW gain and not by their interplay with the modal gain of the particular structure. The abrupt switching from the fundamental mode in regime II to a particular high-order mode in regime I, as reported here in medium-sized devices, is a qualitatively new phenomenon. In these VCSEL's, the mode selection in the respective regimes is determined by an interaction of the spectral gain distribution with the cavity properties. Consequently, existing models successfully used to describe the emission properties of broad aperture devices [20] are not sufficient to describe the features reported here on a quantitative basis. Instead, a more structure-oriented description is required to gain a deeper insight into the interaction of the underlying mechanisms. In the next section, we therefore introduce a detailed electromagnetic model for oxide-confined VCSEL's in the different operating conditions.

III. MODEL

From the results of our experimental investigations, we conclude that the observed emission characteristics are determined by both the cavity geometry and the optical response of the QW's. The spatiospectral interaction of these mechanisms results in the selection of particular transverse modes. We therefore combine in our theoretical approach a model for the cavity transverse modes with a description of the QW's optical gain.

The model for the laser modes is based on a detailed electromagnetic study of the device structure, which yields the spatial field distributions of all cavity modes, their frequency, and their threshold gains. The electromagnetic model, as well as the microscopic model for the spectral gain distribution of the QW's, takes into account all relevant thermal dependences. Thus, the laser threshold conditions at any temperature can be determined by a self-consistent matching of the mode solutions with the gain provided by the QW's at varying pumping, i.e., at varying carrier densities. In this way, the laser threshold mode is found as the mode with lowest threshold carrier density. Since our model does not account for effects such as spatial hole burning and spatial temperature variations, we can apply it to analyze the behavior near threshold. Consequences of this limitation will be discussed in Sec. IV.

A. VCSEL modes

In the following, we refer to the theoretical model presented in [24] in which the laser modes and threshold operating conditions are computed for oxide-confined VCSEL's with complex geometries, starting from the detailed electromagnetic structure of the device and the particular optical response of the QW active material. The adopted model is based on coupled mode theory. The vectorial electromagnetic field is expanded in the continuous basis, $\mathbf{E}_{\alpha plm}(k,\rho,\phi)$, of the cylindrical TE and TM modes of an infinite medium with the characteristics of the passive cavity (their explicit expressions are reported in [30]):

$$\mathbf{E}(\rho,\phi,z)=\sum_{\alpha,p,l,m}\int dk\, A_{\alpha plm}(k,z)\mathbf{E}_{\alpha plm}(k,\rho,\phi), \quad (1)$$

where m labels the discrete azimuthal variation and k is the radial component of the wave vector, which describes the continuous radial variation in terms of Bessel functions; index p refers to the TE and TM distributions, l labels the even and odd modes that differ in their $\sin(m\phi)$ or $\cos(m\phi)$ angular dependence, and $\alpha=f,b$ labels forward and backward propagating waves. In this formalism, it is very easy to derive a linearly polarized (LP) approximation of the modal fields [30]. As shown in detail in [24], this leads to a simplified scalar basis for the field expansion, while the rest of the treatment remains unchanged. In the following, the integral over k is discretized and the vectorial parameter $\mu=(\alpha,p,l,m,k_n)$ is used to label the modes in a compact form: $\mathbf{A}=\{A_\mu \Delta k\}$.

According to the coupled mode theory, all the structural elements that contribute to the lateral optical confinement can be described as transverse perturbations of well defined profile with respect to the homogeneous dielectric constant of the cavity $\varepsilon_c=n_c^2\varepsilon_0$. The vector $\mathbf{A}$ of the mode amplitudes is a solution of the coupled mode equations [31]:

$$\frac{d\mathbf{A}}{dz}=(B+K_i)\mathbf{A}, \quad (2)$$

where B describes the free propagation in the passive cavity material and is a diagonal matrix of elements $-i\beta_\mu$. The longitudinal component of the wave vector is defined as $\beta=\sqrt{k_c^2-k^2}$, where $k_c=n_c\omega/c$. K_i is the matrix of the coupling coefficients and accounts for the perturbation $\Delta\varepsilon_i$ in the layer i. It is a nondiagonal matrix of the form

$$(K_i)_{\mu\mu'}=-\frac{i\omega}{C_\mu}\int\left(\Delta\varepsilon_i\mathbf{E}_{t\mu}\cdot\mathbf{E}_{t\mu'}+\frac{\Delta\varepsilon_i}{\varepsilon_c+\Delta\varepsilon_i}E_{z\mu}E_{z\mu'}\right)dS, \quad (3)$$

where C_μ is the power mode normalization constant, explicitly defined in [24].

In particular, the coupling coefficient matrix related to the active layer accounts for the perturbation induced by the presence of the carriers; we write it as the product of two terms,

$$\Delta\epsilon_a(\rho,\phi)=\Delta\epsilon_a y(\rho,\phi). \quad (4)$$

The peak value of the perturbation, $\Delta\epsilon_a$, is the unknown of the electromagnetic problem and must be determined for every mode by the threshold condition, while the normalized profile of the perturbation, $y(\rho,\phi)$, is related to the carrier profile and is assumed to be a fixed and known function of the system. It is introduced into the model by solving the diffusion equation for the carriers, for a given injection profile and diffusion length. A quantitative estimation of the diffusion length typical for the devices under analysis at low temperatures can be achieved by comparing the numerically obtained carrier profiles with center cuts of the measured near-field profiles below threshold. In our devices we found $L_D=2\ \mu$m.

A formal relation between the amplitudes of backward and forward waves in any two sections of the structure can be obtained as a cascade of single-layer solutions of Eq. (2):

$$\mathbf{A}(z_1) = T\mathbf{A}(z_2) \tag{5}$$

being

$$T = \prod_i \exp(B + K_i) L_i, \tag{6}$$

where the product is carried out for all the layers between z_1 and z_2. In particular, it is convenient to choose the two reference sections as those outside of which the structure is laterally homogeneous, so that it can be treated with the transmission matrix formalism and the related reflectivity coefficients, Γ_u and Γ_l, can be easily calculated as functions of the radial wave vector k. In the case under analysis, for instance, $z_1 = 0$ and $z_2 = L$ are the two interfaces of the lower Bragg mirror with the cavity and of the upper metal ring with air, respectively.

The boundary conditions of the problem are fixed by the consistency of forward and backward waves at the two considered interfaces:

$$\begin{aligned} \mathbf{A}^f(0) &= \Gamma_l \mathbf{A}^b(0), \\ \mathbf{A}^b(L) &= \Gamma_u \mathbf{A}^f(L). \end{aligned} \tag{7}$$

When the formal solution (5) is combined with the imposed boundary conditions (7), the complete electromagnetic problem is formulated and it results in an eigenvalue problem. The eigenvectors of the problem are directly the complex mode amplitudes $\mathbf{A}(0)$. They allow the reconstruction of the field distributions of the different cavity modes at the section $z = 0$, by means of mode expansion (1). The field at any other section of the device is then found by using Eq. (5). On the other hand, the real and imaginary parts of the complex eigenvalue are related, respectively, to the refractive index variation and material gain necessary for each cavity mode to lase.

B. MQW's optical response

In the following, we describe the model adopted for the multiple-quantum-well (MQW) active region and particular attention will be given to describe the thermal dependence of all the parameters. The QW optical response as a function of the frequency ω, the carrier density N, and the temperature is determined by applying the microscopic model (see, for instance, [32]) to the particular QW structure of the device. The obtained expression is of the form

$$\Delta\epsilon_a = \frac{1}{\pi d} \int dk_e \, k_e \frac{M_{k_e}^2}{\hbar} \frac{[f_{ck_e}(N) - f_{vk_e}(N)]}{(\omega_{k_e} - \omega) - i\gamma_p}, \tag{8}$$

where d is the QW thickness, k_e is the carrier wave vector, and γ_p is the polarization relaxation rate. The transition dipole matrix elements (M_k), the transition energies ($\hbar\omega_k$), and the Fermi-Dirac quasiequilibrium distributions in the conduction and valence band (f_{ck}, f_{vk}) have been computed from the QW band structure and depend on the QW composition and size. Coulomb effects are only considered via band-gap renormalization, which varies with carrier density and temperature. Many other parameters in the previous equation depend on temperature. Temperature appears as an explicit variable in the Fermi-Dirac quasiequilibrium distributions, while it implicitly enters the microscopic model through the thermally dependent polarization decay rate and band gap [33]. Since the latter effect is a key element in the model, we report the adopted expression for the band-gap variation with temperature:

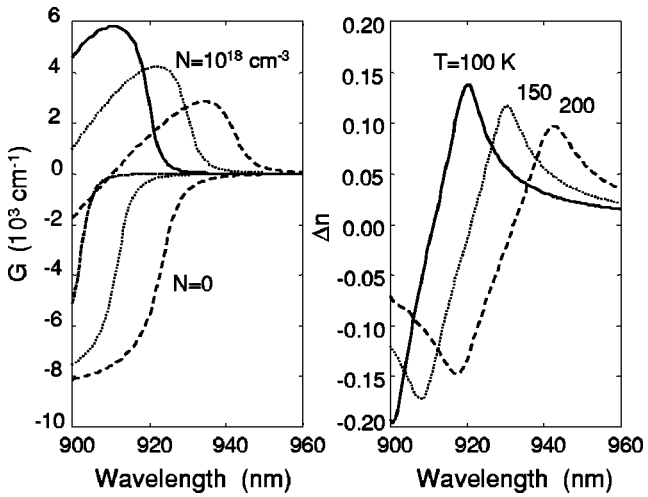

FIG. 7. Gain (left) and refractive index change (right) vs wavelength, for three representative temperatures and two carrier densities; one 8-nm-thick $In_{0.12}Ga_{0.88}As$ QW is considered.

$$E_g(T) - E_g(0) = -\frac{\alpha T^2}{\beta + T}, \tag{9}$$

where the numerical values for $In_{0.12}Ga_{0.88}As$ are taken $\alpha = 4.910^{-4}$ eV/K and $\beta = 220$ K from [33].

Figure 7 shows the calculated spectra of the active material power gain G [Fig. 7(a)] and carrier-induced refractive index change Δn [Fig. 7(b)] at three different temperatures—$T = 100$, 150, and 200 K—for a carrier density of $N = 10^{18}\,\mathrm{cm}^{-3}$ and for zero carriers. For decreasing temperatures, the peaks of the gain curve and of the Δn curve increase and shift to lower wavelengths. The case of zero carriers describes the losses in the QW, which also show a distinct temperature dependence.

The laser operation in a large temperature range can be described if the thermal dependence of all the model parameters is correctly introduced. The change of the cavity properties with temperature is related to the combined effect of mechanical expansion of the layers and refractive index variation [29]. However, since the only quantity that explicitly enters the model is the product $n_i L_i$, it is sufficient to account for the overall effect of the linear shift of the cavity resonances. The value of the linear coefficient has been estimated from the experimentally measured optical spectra by performing a fit of the mode peak shift with temperature. The obtained values are 0.050 nm/K in the low-temperature regime and 0.055 nm/K in the high-temperature regime.

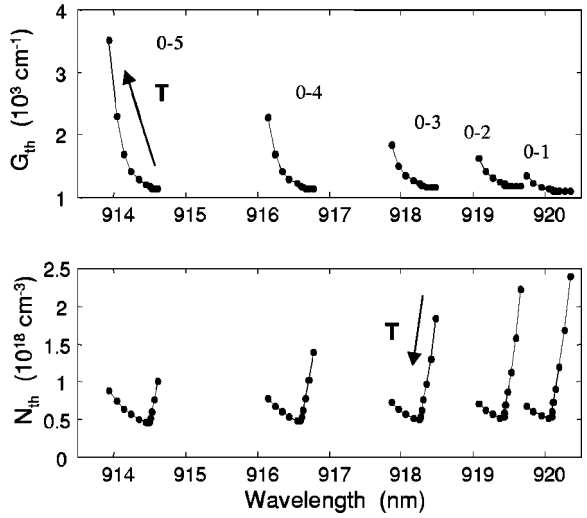

FIG. 8. Threshold gains, carrier densities, and wavelengths as a function of temperature for the modes with zero azimuthal variation.

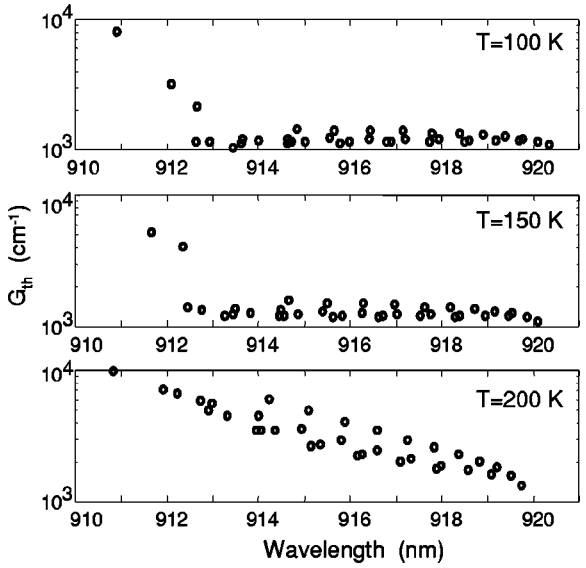

FIG. 9. Power threshold gains and wavelengths of the modes for $T=100$, 150, and 200 K in logarithmic scale.

IV. NUMERICAL RESULTS AND DISCUSSION

In this section, we present our numerical simulation of the VCSEL emission characteristics. The results have been obtained by applying the above-described model to the particular VCSEL structure under analysis. We compared the results of both the vectorial and scalar models and we obtained only small quantitative differences; so, because in this context we are not interested in mode polarization analysis, we adopt the approximated scalar approach to reduce the numerical effort. A more detailed discussion on the limits of application of the LP approximation can be found in [24]. The electromagnetic model provides as solutions the cavity modes of the particular VCSEL that are characterized by wavelengths, spatial field profiles, and threshold gain values. The mode solutions are combined with the QW optical gain spectrum in a self-consistent way. The laser threshold solution is then determined by the cavity mode, whose threshold gain matches the QW gain at the lowest carrier density.

To give a first overview over the laser mode solutions and their thermal dependence, as an example we plot in the upper part of Fig. 8 the threshold power gain versus wavelength of five selected modes (0-1, 0-2, 0-3, 0-4, and 0-5) for 11 values of temperature from 100 to 200 K. The modes are labeled according to the LP notation where the couples of numbers *m*-*n* indicate the mode azimuthal and radial orders, respectively. The first effect we observe under increasing temperature is a blueshift of all modes. This dispersive behavior is related to the carrier-induced change of refractive index, reported in Fig. 7. Second, the threshold power gains of all modes increase due to the thermal variation of the QW losses also depicted in Fig. 7. The rate of increase is significantly larger for modes at lower wavelengths, so that low-order modes (i.e., longer wavelengths) have the lowest threshold gain at high temperature. At low temperatures, in contrast, the threshold gain of all modes appears to be of comparable size. Since the QW gain curve has a pronounced spectral variation, it must be emphasized once more that the laser threshold solution is not determined by the mode of lowest threshold gain, but by the mode of lowest threshold carrier density. The threshold carrier densities are depicted in the lower part of Fig. 8. It is evident that higher-order modes are strongly favored in the low-temperature regime due to their lowest threshold carrier densities. At high temperatures, in contrast, we find only a slight preference of low-order modes, so that in this regime, a stronger mode competition has to be expected. Moreover, the different minima at the respective temperatures indicate when the individual modes match the QW gain maximum. Figure 8, however, serves only for a general overview over the threshold conditions of some involved modes and their general thermal dependences. An analysis of the laser operation requires us to consider all relevant modes, as will be done in the following.

The threshold power gains and wavelengths of all supported cavity modes are summarized in Fig. 9 for three fixed values of temperature, $T=100$, 150, and 200 K. The threshold power gain distributions provide information on the number and wavelength range of the supported VCSEL modes. Referring to $T=100$ K, the upper limit of the mode spectral distribution is set by the wavelength of the fundamental mode, $\lambda_{II}=920.5$ nm, while the lower limit to the laser emission wavelength is found at $\lambda_I=913$ nm, where the abrupt increase in mode threshold gain indicates the loss of transverse confinement. In the interval between λ_I and λ_{II}, all the modes are well confined within the oxide aperture and thus the threshold gain distribution is almost constant. We find $\lambda_{II}-\lambda_I=7.5$ nm, in excellent agreement with the experimentally observed 7.4 nm spectral gap in the laser emission. According to the thermal evolution of the mode gains, as shown in Fig. 8 exemplarily for only five selected modes, the threshold gains of all modes increase with temperature. The different rates lead to an increasing preference of the low-order modes at high temperature, as is evident when comparing the $T=150$ K case with the one at $T=200$ K. At $T=200$ K, the threshold gains for the modes around λ_I are

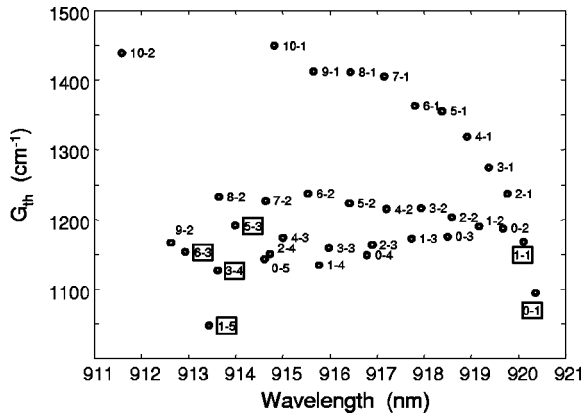

FIG. 10. Expanded depiction of the mode threshold gains at $T = 100$ K; the modes marked by a box are the ones found in the experiment.

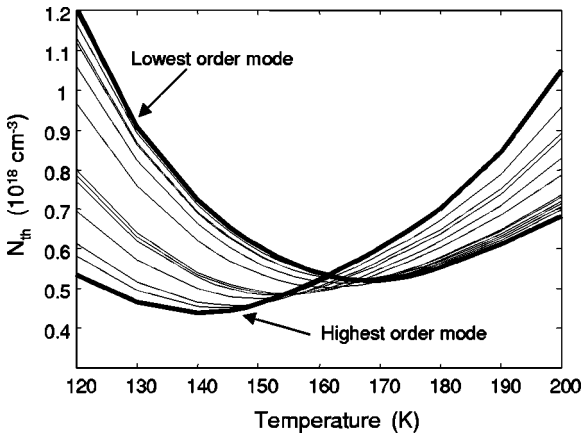

FIG. 11. Threshold carrier density vs temperature for the relevant different VCSEL modes.

almost one order of magnitude larger than for modes around λ_{II}. These results already provide the two wavelength limits for the laser emission: the mode of highest wavelength is always the fundamental mode, which is favored at high temperatures. A distinct low-wavelength limit at low temperatures is set by a strong increase in gain for modes of $\lambda < 913$ nm. At high temperatures instead, the increase of threshold gain is rather gradual, so that one expects to find high-order modes lasing at increased injection currents due to Joule heating. Since the gain distribution of the modes between λ_I and λ_{II} is not clearly evident from the given depiction, we present the threshold gains for the cavity modes at $T = 100$ K in an expanded representation in Fig. 10. From this depiction, it is evident that modes near the two wavelengths $\lambda_I = 913$ nm and $\lambda_{II} = 920.5$ nm have a lower threshold gain than all other cavity modes. For modes around $\lambda_{II} = 920.5$ nm, i.e., low-order transverse modes, threshold gains are reduced due to the better overlap of their intensity distributions with the spatial gain distribution, peaked at the center of the laser for low pump currents. This results as a solution of the transverse diffusion equation in agreement with experimental observations [12]. The gain of high-order modes instead is determined by a different mechanism: the oxidation of the AlAs layer in the upper mirror decreases the optical index in the confinement region at the periphery of the VCSEL to $n \approx 1.6$. Thus, the reflectivity of the upper mirror is locally increased due to the enhanced contrast between the optical index of the adjacent layers. This local higher reflectivity is more efficient on the higher-order modes that exhibit higher transverse components of the k vector, and thus the threshold gain of these modes around $\lambda_I = 913$ nm is reduced. As mentioned before, modes of even shorter wavelength, i.e., of higher order, have strongly increased threshold gains due to a loss of transverse confinement, because their spatial extension exceeds the area of the oxide aperture.

It has to be emphasized that the results obtained in Fig. 10 are sensitive to the technological device construction characteristics. In particular, the number and wavelength range of the confined modes critically depend on the position, thickness, and the index step of the oxide layer. High-order mode emission under these conditions can therefore be described only by rigorous electromagnetic modeling.

By combining the data of Fig. 10 with the QW spectral gain distribution, we determine the threshold carrier densities of the laser modes at any temperature, as explained in the context of Fig. 8. The threshold carrier densities of the most relevant cavity modes are reported versus temperature in Fig. 11, where the curves corresponding to the lowest- and highest-order mode, dominant in regime I and regime II, are indicated with the bold lines. In this way, the thermal dependence of the laser threshold is directly obtained and finally depicted in Fig. 12. The currents of the primary laser threshold (i.e., the threshold of the first lasing mode) and of the secondary laser threshold (i.e., the threshold of the fundamental transverse mode) are shown, according to the same notation adopted in Fig. 3. The experimental data are superimposed with bold symbols onto the numerical ones (open symbols). The primary laser threshold current is obtained from the lower envelope of the curves in Fig. 11, indicating the mode with the lowest threshold carrier density. The adopted conversion relation is $I_{th} = CN_{th}$, where C is ob-

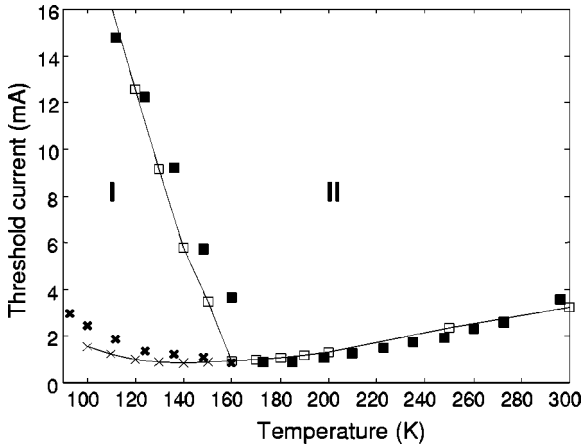

FIG. 12. Computed (open symbols) and measured (bold symbols) threshold currents vs temperature in the two operating regimes; squares indicate low divergence emission (regime II) while crosses characterize high divergence modes (regime I).

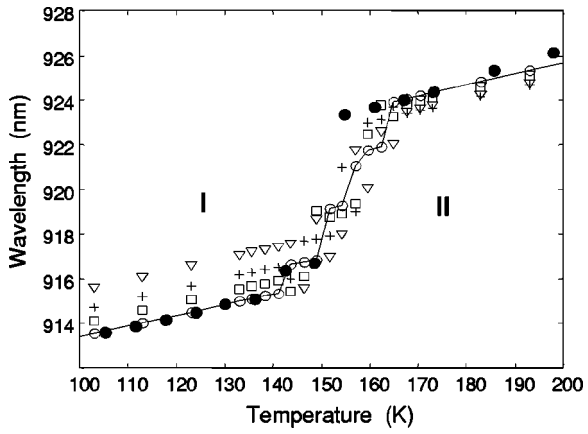

FIG. 13. Temperature dependence of the wavelength of the first four modes ordered with respect to the threshold carrier density. Lowest threshold carrier density is denoted by open circles connected by the solid line; open squares, plus signs, and open triangles refer to increasing densities. The full circles correspond to the strongest laser mode found in the experiment.

tained by comparing the experimental I_{th} and theoretical N_{th} values at their minima. From the relation $C=qV/\tau$, where q is the unit charge, V is the active volume, and τ is the carrier recombination lifetime, we obtained $\tau=0.2$ ns, a reasonable value for this material. The agreement between experimental and numerical results is very good and only a slight mismatch between the positions of the threshold minima and of the values at low temperature is observed. This can be attributed to the very simple carrier density to current conversion relation adopted, where the temperature dependence of τ and of the carriers transverse diffusion length has been neglected.

In the same figure, we also depict the current value at which the emission on the low-order modes starts (upper branch). This occurs when the current-induced heating raises the laser internal temperature from ambient temperature to a critical temperature T_c at which the threshold carrier density of the lasing mode is equal to that of the lowest-order mode (see Fig. 11). The value of T_c is constant in regime I ($T<140$ K), where emission occurs on one fixed mode, while it becomes a function of temperature in the transition region ($T=140-165$ K), where the laser switches with temperature through several modes. The relation describing the current-induced heating is determined by combined measurements of mode shifts with temperature and current, and we found $\Delta T=\theta\Delta I$, with $\theta\simeq 3$ K/mA. The spacing between the two mode thresholds is therefore obtained by the relation $I_{\mathrm{th,II}}-I_{\mathrm{th,I}}=-(T-T_c)/\theta$, which is linear only up to $T=140$ K. The obtained borders of the two regimes are in close agreement with the experimental observations. Since spatial and spectral hole burning are not considered in our model, we conclude that these effects do not play a fundamental role in the operation regimes under investigation, and thus the adopted model is suitable for an identification of the mechanisms underlying the transverse mode selection.

Next, we compare the spectral properties of the modeled laser operation to the experimental observations. In Fig. 13, we depict the calculated wavelengths of the four modes with lowest threshold carrier densities as a function of temperature between $T=100$ and 200 K. These are superimposed with the strongest mode in the experimentally measured optical spectra close to threshold (cf. Fig. 6). The different symbols adopted to order the modes are explained in the figure caption and the line connects the mode with lowest threshold as obtained from the numerical results.

For low temperatures up to $T=140$ K, lasing operation is stable on one particular mode at λ_{I} (regime I), in perfect agreement between model and experiment. The continuous variation of the mode wavelength is only related to the thermally induced shift of the longitudinal cavity resonance at an overall rate of $+0.050$ nm/K, determined by both the cavity mechanical expansion coefficient and the refractive index thermal variation rate. At temperatures between $T=140$ and 165 K, the transition to regime II occurs, in which we find stable operation on the fundamental mode at λ_{II} from $T=165$ K up to room temperature. Again, the calculated emission wavelength well matches the observed laser operation. The only slight discrepancy between model and experiment is observed during the transition. First, between $T=140$ and 145 K, both measured and calculated data show a mode jump to a longer wavelength by $+1.3$ nm. Then, the numerical results describe a transition scenario where a few modes at intermediate wavelengths around 919 and 921 nm are involved at temperatures between $T=150$ and 165 K. The measured emission instead changes abruptly to the fundamental mode at $T=150$ K. This deviating behavior finds an explanation in dynamical mechanisms, which make the system unstable in the transition regime and cannot be accounted for in the model: the considered temperature range is dominated by a very strong competition among several modes of comparable threshold carrier densities, as can be clearly seen in Fig. 11. While outside this region the model describes very well the emission properties, around the switching temperature effects such as spatial and spectral hole burning contribute to the mode competition, so that the calculated lowest threshold modes at intermediate wavelengths become unstable in favor of modes around either λ_{I} or λ_{II}. Indications of such instabilities have also been observed experimentally: at temperatures around $T=150$ K, i.e., close to the transition, an ''anomalous'' switching between the regimes has been found. This means that with increasing injection current, the laser changes from regime II to regime I and back to regime II again, which is further evidence for a strong mode competition.

The abrupt switching described above is strongly related to the mode threshold gain spectral distribution (see Fig. 10), which again is sensitive to changes of the transverse device structure: for increasing diameter, the gain differences between the respective modes become smaller and their distribution tends to flatten. This is a result of the decreasing influence of the transverse optical confinement by the oxide layer. Consequently, the wavelength transition becomes smoother, now mainly determined by the active material spectral shift. We have observed such behavior in VCSEL's with the same geometry but larger oxide aperture diameter ($d\approx 34\,\mu$m): for low temperatures, emission wavelength shifted continuously at a rate larger than the one determined by the thermal shift of the cavity resonance. A spectral gap

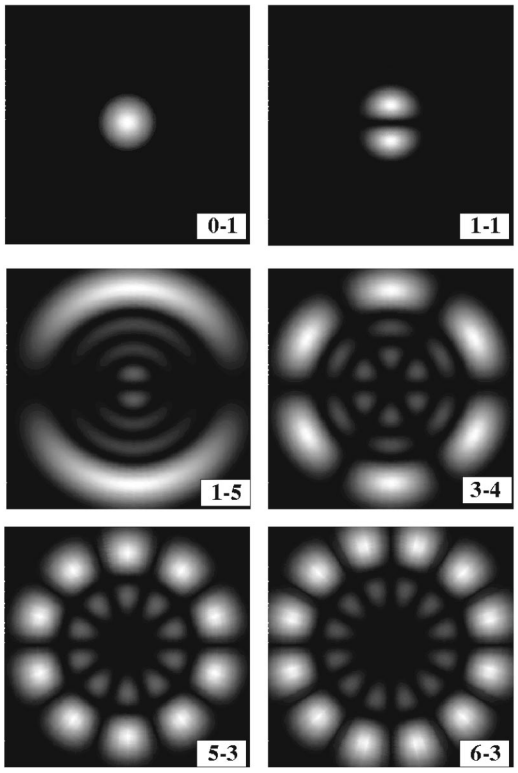

FIG. 14. Computed far-field distributions for the modes involved in the laser emission. The image sizes are 12 cm and are computed at 10 cm from the VCSEL output.

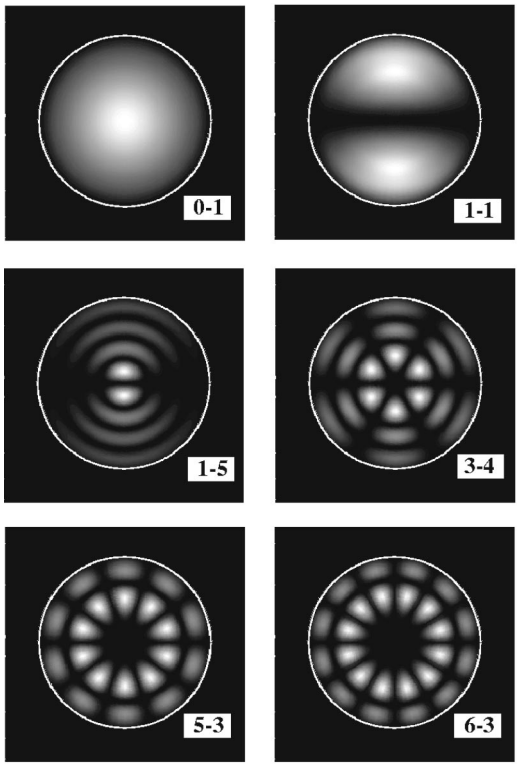

FIG. 15. Computed near-field distributions corresponding to the far fields of Fig. 14; the white circle indicates the aperture of the metal contact 8.6 μm in diameter.

or an upper limit to the far-field divergence angle (corresponding to an upper limit to the mode radial order) was not observed in the accessible detuning range, similar to the behavior reported in [18,19].

Apart from threshold carrier density and operation wavelength, the model also provides the spatial field distribution and the *k*-vector distributions of the modes. For a comparison with the measured data, we first consider the far-field intensity distributions. The calculated far fields are depicted in Fig. 14 for the modes 0-1 and 1-1, dominant in the high-wavelength region around λ_{II}, and the modes 1-5, 3-4, 5-3, and 6-3 having lowest threshold around λ_I. The LP treatment results in sets of modes degenerate in polarization and spatial symmetry (fourfold degeneracy); we show only one example of each set. The modes 0-1 and 1-1 have comparable threshold carrier densities and, therefore, already slightly above threshold, both contribute to the laser emission. Therefore, the superposition of the calculated modes 0-1 and 1-1 results in a far-field distribution very similar to the experimentally observed one in Fig. 4(e). In particular, the computed full divergence angles of the two modes, 16° and 22°, coincide with the measured divergence in the horizontal and vertical directions. Furthermore, also the superposition of the four high-order modes reproduces well the measured far field of regime I in Fig. 4(a): the number of rings (four) determined by the mode of highest radial order as well as the divergence of the outmost ring (70°) are in exact agreement. The almost constant divergence of the four significant modes around λ_I is related to the similar value of the transverse wave vector.

Figure 15 depicts the calculated near-field distributions for the same modes as in Fig. 14. As in Fig. 4, the white circle indicates the aperture of the metal contact ring. A superposition of the modes 0-1 and 1-1 describes well the experimentally observed emission in regime I, shown in Fig. 4(f). Emission in regime II [Fig. 4(b)] is reproduced by the superposition of the four high-order modes around λ_I. This is even more visible when experimentally discriminating subsets of these modes by insertion of a polarizer. The polarization resolved near fields are plotted in Fig. 16. The 0° polarized near field (left part of Fig. 16) is a superposition of the bow-tie structure of mode 1-5 and the 10-lobed structure of mode 5-3. Furthermore, the 6- and 12-lobed structure of

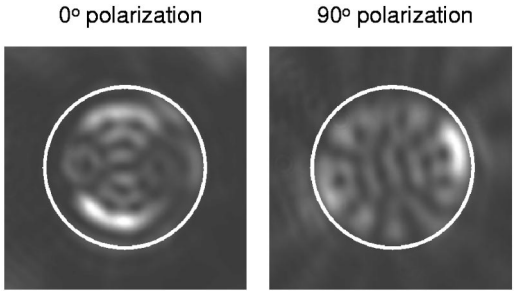

FIG. 16. Experimental near-field images for the two orthogonal polarizations; $T=100$ K and $I=5$ mA for 0° polarization, $T=125$ K and $I=6$ mA for 90° polarization.

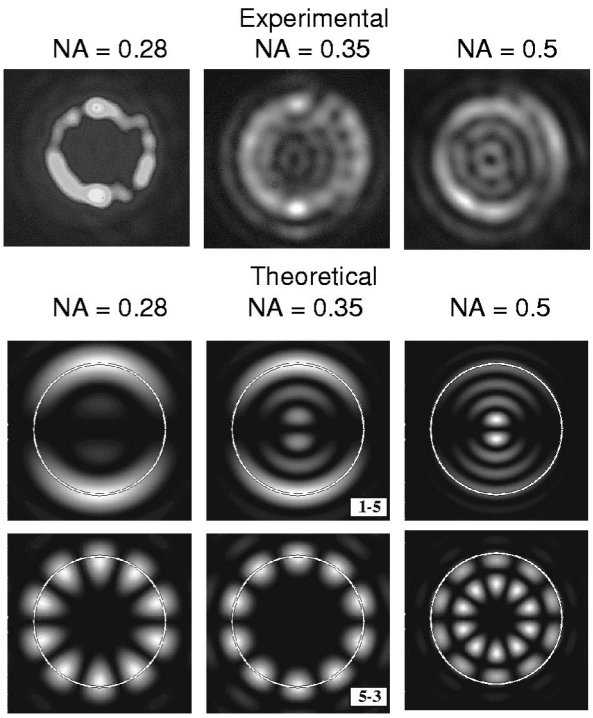

FIG. 17. Experimentally observed and computed effect of numerical aperture limitations on the near-field images.

modes 3-4 and 6-3 together with the 1-5 mode aligned along the horizontal axis govern the 90° polarization (right part of Fig. 16).

In addition, as has been mentioned already in Sec. II A, the accuracy of the measured near-field images might be limited by an insufficient numerical aperture of the used objectives. In that case, the fraction of the emitted light with the largest transverse k vector would be selectively blocked. In order to quantify the effect of this limitation and to estimate the accuracy of the measured near-field images, we compare in Fig. 17 experimental near-fields images, measured with objectives of different NA (upper part), and calculated near fields of the modes 1-5 and 5-3, where a cutoff has been performed at the transverse k vector that corresponds to the NA limitation of the respective objective (lower part). The main effect of a reduced numerical aperture is a suppression of the inner structure of the near field. At a NA of 0.5, however, as used in the experiments, the distortions are only weak, and the agreement between the calculated exact modes of Fig. 15 and the experimental ones of Fig. 16 remains unaffected.

V. CONCLUSIONS

We have presented a comprehensive analysis of the emission behavior of medium-sized oxide-confined VCSEL's under variation of the operation temperature. As the characteristic feature, we have found a thermally controlled transition between two distinct regimes with fundamentally different spectral and spatial emission properties. In either of these emission regimes, the limits towards long and short wavelengths are determined by the fundamental transverse mode or by a particular transverse mode of high radial order. The abrupt transition between the regimes is the result of the combined effect of the thermally induced detuning and the oxide-layer-specific optical confinement, which is most efficient on high-order transverse modes. Insight into these basic laser-optic mechanisms has been achieved by modeling the detailed electromagnetic structure of the device and the QW optical response, including the thermal dependence of all relevant parameters. The obtained numerical results are in excellent agreement with the experimental observations. In particular, the spectral and spatial emission characteristics in the two regimes, the spectral gap between the regimes, and the critical temperature of the transition are quantitatively reproduced. These results relate the lasing properties to the particular device construction characteristics and therefore offer the perspective to control and to utilize the high-order mode emission.

ACKNOWLEDGMENTS

The activity reported has been carried out in the framework of the Vigoni project (DAAD/CRUI). The Torino group acknowledges the support of MADESS II (Progetto Finalizzato of Italian CNR). The Darmstadt group acknowledges funding by Deutsche Forschungsgemeinschaft (EL 105/10).

[1] K. J. Ebeling, U. Fiedler, R. Michalzik, G. Reiner, and B. Weigl, Int. J. Electron. Commun. **50**, 316 (1996).
[2] Kirk S. Giboney, Lewis B. Aronson, and Brian E. Lemoff, IEEE Spectr. **2**, 43 (1998).
[3] *Vertical-Cavity Surface-Emitting Lasers*, edited by C. Wilmsen, H. Temkin, and L. A. Coldren (Cambridge University Press, New York, 1999).
[4] K. D. Choquette, R. P. Schneider, K. Lear, and K. Geib, Electron. Lett. **30**, 2043 (1994).
[5] C. Degen, J.-L. Vey, W. Elsäßer, P. Schnitzer, and K.-J. Ebeling, Electron. Lett. **34**, 1585 (1998).
[6] J. L. Vey, C. Degen, K. Auen, and W. Elsäßer, Phys. Rev. A **60**, 3284 (1999).
[7] G. P. Bava, L. Fratta, and P. Debernardi, J. Opt. Soc. Am. B **16**, 2147 (1999).
[8] M. San Miguel, Q. Feng, and J. V. Moloney, Phys. Rev. A **52**, 1728 (1995).
[9] M. P. van Exter, M. B. Willemsen, and J. P. Woerdman, Phys. Rev. A **58**, 4191 (1998).
[10] S. Balle, E. Tolkachova, M. San Miguel, J. R. Tredicce, J. Martin-Regalado, and A. Gahl, Opt. Lett. **24**, 1121 (1999).
[11] M. Brambilla, L. A. Lugiato, F. Prati, L. Spinelli, and W. J. Firth, Phys. Rev. Lett. **79**, 2042 (1997).
[12] C. Degen, I. Fischer, and W. Elsäßer, Opt. Express **5**, 38 (1999).
[13] T. Milster, W. Jiang, E. Walker, D. Burak, P. Claisse, P. Kelly,

and R. Binder, Appl. Phys. Lett. **72**, 3425 (1998).
[14] K. H. Hahn, M. R. Tan, Y. M. Houng, and S. Y. Wang, Electron. Lett. **29**, 1482 (1993).
[15] Y. Kaneko, T. Tamanuki, M. Katoh, H. Maekawa, F. Koyama, and K. Iga, Jpn. J. Appl. Phys., Part 2 **32**, L1612 (1993).
[16] T. J. Rogers, D. L. Huffaker, H. Deng, Q. Deng, and D. G. Deppe, IEEE Photonics Technol. Lett. **7**, 238 (1995).
[17] C. H. McMahon, J. W. Bae, C. S. Menoni, D. Patel, H. Temkin, P. Brusenbach, and R. Leibenguth, Appl. Phys. Lett. **66**, 2171 (1995).
[18] S. P. Hegarty, G. Huyet, J. G. McInerney, and K. D. Choquette, Phys. Rev. Lett. **82**, 1434 (1999).
[19] S. P. Hegarty, G. Huyet, P. Porta, J. G. McInerney, K. D. Choquette, K. M. Geib, and H. Q. Hou, J. Opt. Soc. Am. B **16**, 2060 (1999).
[20] T. Rössler, R. A. Indik, G. K. Harkness, J. V. Moloney, and C. Z. Ning, Phys. Rev. A **58**, 3279 (1998).
[21] G. M. Yang, M. H. MacDougal, and P. D. Dapkus, J. Appl. Phys. **80**, 4837 (1996).
[22] D. L. Huffaker, H. Deng, Q. Deng, and D. G. Deppe, Appl. Phys. Lett. **69**, 3477 (1996).
[23] P. Dowd, L. Raddatz, Y. Sumalia, M. Asghari, I. H. White, R. V. Penty, P. J. Heard, G. C. Allen, R. P. Schneider, M. R. T. Tan, and S. Y. Wang, IEEE Photonics Technol. Lett. **9**, 1193 (1997).
[24] G. P. Bava, P. Debernardi, and L. Fratta, preceding paper, Phys. Rev. A **63**, 023816 (2001).
[25] S. Eitel, S. J. Fancey, H-P. Gauggel, K-H. Gulden, W. Bächthold, and M. R. Taghizadeh, IEEE Photonics Technol. Lett. **12**, 459 (2000).
[26] T. A. Richard, S. A. Maranowski, N. Holonyak, Jr., E. I. Chen, and M. J. Ries, Appl. Phys. Lett. **66**, 886 (1995).
[27] T. R. Nelson, Jr., J. P. Prineas, G. Khitrova, H. M. Gibbs, J. D. Berger, and E. K. Lindkmark, Appl. Phys. Lett. **69**, 3031 (1996).
[28] D. L. Huffaker, D. G. Deppe, and T. J. Rogers, Appl. Phys. Lett. **65**, 1611 (1994).
[29] J. Piprek, H. Wenzel, and G. Sztefka, IEEE Photonics Technol. Lett. **6**, 139 (1994).
[30] A. W. Snyder and J. D. Love, *Optical Waveguide Theory* (Chapman and Hall, London, 1983).
[31] D. Marcuse, *Theory of Dielectric Waveguides* (Academic, Boston, 1974).
[32] P. Debernardi, A. Pisoni, and G. P. Bava, IEEE J. Quantum Electron. **30**, 93 (1994).
[33] Z. Hang, D. Yan, F. H. Pollak, G. D. Pettit, and J. M. Woodall, Phys. Rev. B **44**, 10 546 (1991).